Photoexcited charge carrier dynamics in Sb2Se3(100)

Grad, Lisa ; von Rohr, Fabian ; Zhao, Jianzhou ; Hengsberger, Matthias ; Osterwalder, Jürg

Abstract: Antimony selenide (Sb2Se3) consists of one-dimensional ribbons that are van der Waals bonded to each other. Due to its favorable optoelectronic properties, it is a promising material for solar energy conversion. Owing to its narrow direct band gap and its high absorption coefficient it is an efficient absorber for solar light. Besides, it is cheap, stable in harsh environments, and abundant with low toxicity. For its use in solar devices, efficient transport of photoexcited charge carriers towards the active interface and long lifetimes at sufficiently high energies are mandatory. Here time-resolved two-photon photoemission experiments on the (100) surface of Sb2Se3 are presented. Data were taken along and perpendicular to the direction of the one-dimensional ribbons in order to unravel the anisotropic lifetimes and relaxation dynamics of photoexcited charge carriers. In both cases, various conduction bands could be populated and within the first picosecond ultrafast scattering towards the lowest conduction band was observed. Moreover, long lifetimes of up to 35 ps in the conduction band bottom at the surface were obtained and no sign of trapping in defect states was found. These measurements shed light on the relaxation and scattering of free carriers in Sb2Se3, which is the key for the design of Sb2Se3-based electrodes.

DOI: https://doi.org/10.1103/PhysRevMaterials.4.105404

Photoexcited charge carrier dynamics in Sb_2Se_3(100)

Lisa Grad [1,*] Fabian von Rohr,[2] Jianzhou Zhao,[3,4] Matthias Hengsberger [1] and Jürg Osterwalder [1]

[1]*Department of Physics, University of Zurich, Winterthurerstrasse 190, 8057 Zurich, Switzerland*
[2]*Department of Chemistry, University of Zurich, Winterthurerstrasse 190, 8057 Zurich, Switzerland*
[3]*Co-Innovation Center for New Energetic Materials, Southwest University of Science and Technology, Mianyang, 621010, People's Republic of China*
[4]*Research Laboratory for Quantum Materials, Singapore University of Technology and Design, Singapore 487372, Singapore*

(Received 10 August 2020; accepted 7 October 2020; published xxxxxxxxxx)

Antimony selenide (Sb_2Se_3) consists of one-dimensional ribbons that are van der Waals bonded to each other. Due to its favorable optoelectronic properties, it is a promising material for solar energy conversion. Owing to its narrow direct band gap and its high absorption coefficient it is an efficient absorber for solar light. Besides, it is cheap, stable in harsh environments, and abundant with low toxicity. For its use in solar devices, efficient transport of photoexcited charge carriers towards the active interface and long lifetimes at sufficiently high energies are mandatory. Here time-resolved two-photon photoemission experiments on the (100) surface of Sb_2Se_3 are presented. Data were taken along and perpendicular to the direction of the one-dimensional ribbons in order to unravel the anisotropic lifetimes and relaxation dynamics of photoexcited charge carriers. In both cases, various conduction bands could be populated and within the first picosecond ultrafast scattering towards the lowest conduction band was observed. Moreover, long lifetimes of up to 35 ps in the conduction band bottom at the surface were obtained and no sign of trapping in defect states was found. These measurements shed light on the relaxation and scattering of free carriers in Sb_2Se_3, which is the key for the design of Sb_2Se_3-based electrodes.

DOI: 10.1103/PhysRevMaterials.00.005400

I. INTRODUCTION

The conversion and storage of solar energy is an important step towards sustainable energy production. In solar devices, light is absorbed in a semiconducting material leading to the generation of electron-hole pairs. These need to be separated and transferred to a specific region in the device before recombination occurs. At an interface, the chemical potentials of the adjacent materials equilibrate due to charge carrier diffusion across the interface. The accompanying electric built-in field is used to separate the photogenerated electron-hole pairs. In a photovoltaic cell, the charge carriers are transferred to an external circuit, while in a photoelectrochemical cell they are injected into an electrolyte. There they drive chemical redox reactions that store energy in chemical bonds, for instance via the production of hydrogen from water. These concepts are viable at the large scale if electrodes with high conversion efficiencies can be built from cheap, earth-abundant, and nontoxic materials that are stable under working conditions.

A promising material for solar energy conversion is the *p*-type semiconductor antimony selenide (Sb_2Se_3). Due to its narrow band gap of 1.0 eV and its high absorption coefficient, it is a good absorber for solar light [1]. Besides, it shows low toxicity, and due to its binary composition, it can be synthesized at low temperature with a good control over its phase and stoichiometry [1]. It consists of one-dimensional covalently bonded $(Sb_4Se_6)_n$ ribbons which are in turn bonded by weaker van der Waals forces [2–4]. The crystal structure with the orthorhombic unit cell, the Brillouin zone and a light microscope image of Sb_2Se_3 are depicted in Figs. 1(a)–1(c). The strong structural anisotropy is also reflected in the optical [5] and transport [6,7] properties of this material. Moreover, the one-dimensional structure and the van der Waals bonding make sure that the bonds at the grain boundaries are saturated that reduces recombination losses [8].

Sb_2Se_3 was first introduced to photovoltaics by Nair *et al.* in 1999 [9]. Since then, the highest efficiencies of 9.2% [10,11] were obtained in thin-film solar cells consisting of Sb_2Se_3 nanorod arrays where the ribbon direction is normal to the surface. This enables efficient charge carrier transport along the ribbon direction and the nanostructured morphology allows to match the nanorod length to the optical absorption length while increasing massively the active surface area. Additionally, the size of the nanostructures was matched to the charge carrier diffusion length so that a large part of the photogenerated charge carriers could be transferred to the surface. The charge transfer across the junction could be improved by a thin TiO_2 interlayer that prevented the intermixing of Sb_2Se_3 and a CdS buffer layer. Owing to such measures, high photocurrents and good stability properties could be achieved. Nevertheless, the efficiencies are still below those of competing systems like hybrid organic-inorganic perovskite solar cells [12,13] or Cu_2O-based photocathodes for water splitting [14,15], and the open circuit voltage is rather low.

*Corresponding author: lisagrad@physik.uzh.ch

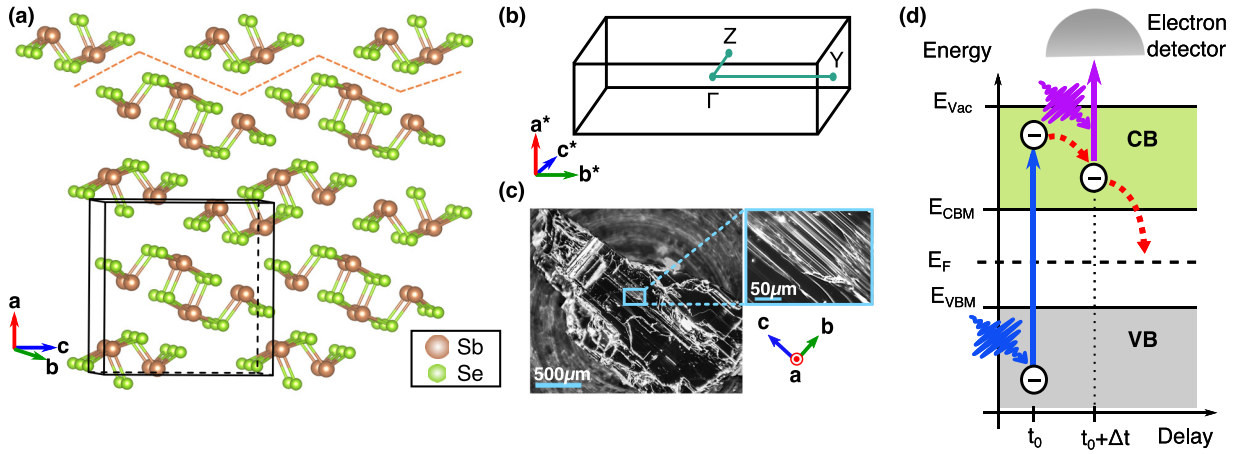

FIG. 1. (a) Crystal structure of Sb_2Se_3 with the cleavage plane (orange dashed line) and the orthorhombic unit cell marked. The ribbons run along $\vec{b}$ and are shown in cross-sectional view. Sb atoms are colored in brown and Se atoms in green. (b) Brillouin zone of Sb_2Se_3 with the directions along ribbons (ΓY) and across ribbons (ΓZ) indicated. (c) Light microscope image of the Sb_2Se_3 sample (brightness and contrast processed). $\vec{a}$ denotes the surface normal, $\vec{b}$ the direction along, and $\vec{c}$ across the ribbons. (d) Schematic energy level diagram of Sb_2Se_3 and principle of tr-2PPE. By absorption of a pump photon electrons are excited from the VB to the CB. The excited electrons are emitted by absorption of a probe photon and can be detected according to energy and momentum. By applying a defined time delay between excitation and emission, the relaxation processes can be investigated.

In order to identify losses that occur in Sb_2Se_3 photoelectrodes the dynamics of charge carriers after photoexcitation need to be investigated. Efficient bulk-to-surface transport and charge injection into adjacent media have to take place before recombination occurs. Furthermore, photoexcited charge carriers can be trapped in interfacial and bulk defects, which form states within the band gap. Such trapping dissipates an important part of the energy of the charge carriers and results in large photovoltage losses. Moreover, it strongly reduces the carrier mobilities because thermal-assisted hopping between equivalent defect sites is the only possible transport mechanism.

In a recent study Yang *et al.* have investigated the charge carrier dynamics on nanostructured low-cost $Sb_2Se_3/TiO_2/RuO_x$ photocathodes over the full pico- to microsecond timescale [16]. Based on time-resolved terahertz spectroscopy measurements, a charge carrier relaxation within 10–30 ps after optical excitation is reported. Due to the observed dependence of the decay time on the excitation density this could be attributed to an interaction between excited charge carriers. In time-resolved photoluminescence measurements, a nonradiative decay into defect states within $\tau_1 \approx 0.15$ ns was observed. By means of intensity-modulated photocurrent and photovoltage spectroscopy the surface recombination rate and the charge injection rate into the electrolyte were studied. Both of these factors could be improved when a RuO_x co-catalyst layer was used, and the low photovoltages could be attributed to a sluggish charge transfer rather than to fast surface recombination.

More recently, time-resolved terahertz and transient absorption spectroscopy measurements were conducted on polycrystalline Sb_2Se_3 thin films in Ref. [17]. The authors observed nonthermalized electrons during the first 130 fs after photoexcitation, followed by hot-carrier cooling within the subsequent 350 fs. A decay of the conduction band population into bulk defects within 23 ps is reported, where they have a long lifetime of 59 ns. Measurements for different thin-film thicknesses showed that the relaxation of photoexcited charge carriers into defects is unaffected by the surface, whereas the lifetime in defect states is determined by surface recombination. Furthermore, the diffusion length for free and trapped charge carriers were determined and it was found that both carrier types contribute to the photocurrent. As a consequence, the losses that occur on Sb_2Se_3 photoelectrodes were attributed to charge carrier trapping in defect states.

However, these experiments provide no information about the time-dependent energy and momentum distribution of photoexcited charge carriers. Thus their time constants cannot be attributed to distinct electronic states or transitions. In addition, anisotropic phenomena due to the one-dimensional ribbon structure of Sb_2Se_3 have not been investigated so far. Moreover, in order to assess whether their results can be transferred to other Sb_2Se_3-based electrodes, the influence of the nanostructured morphology, and the polycrystalline structure on the charge carrier dynamics have to be addressed.

Time- and angle-resolved two-photon photoemission (tr-2PPE) is an appropriate tool to investigate the charge carrier dynamics in Sb_2Se_3 with momentum resolution. In this surface-sensitive technique, absorption of a pump photon leads to excitation of an electron from the valence band (VB) to the conduction band (CB) from where it can be photoemitted by a probe photon and detected according to energy and momentum. In this way, the conduction band electronic structure can be monitored. In addition, by applying a well defined time delay between excitation and photoemission, the relaxation dynamics of the excited states can be investigated on a femto- to picosecond timescale. The principle of tr-2PPE is shown in Fig. 1(d). It was already successfully applied to study Cu_2O photocathodes [18]. The probing depth of tr-2PPE is much more shallow than the light absorption length and

the depth of the surface depletion region. Thus the measured signal is a superposition of direct transitions within the near-surface region and the transport of charge carriers towards the surface due to the built-in field.

Here tr-2PPE measurements are presented from the (100) surface of cleaved Sb_2Se_3 single crystals. Two distinct crystallographic directions along and perpendicular to the direction of the one-dimensional ribbons are compared, corresponding to ΓY and ΓZ, respectively. In this way, we are able to investigate effects of the structural anisotropy on the unoccupied electronic structure and the charge carrier dynamics. In both cases, photoexcitation leads to the population of the same manifold of conduction bands. Within the first 600 fs scattering towards the lowest conduction band arises, followed by momentum scattering towards band minima along ΓY and ΓZ in the subsequent picosecond. At the band minima, rather long lifetimes of 25 and 35 ps were observed at ΓY and ΓZ, respectively. No evidence for charge carrier trapping in surface defect states was found. These results support the suitability of Sb_2Se_3 for solar energy conversion.

II. EXPERIMENTAL AND THEORETICAL METHODS

A. Crystal growth

The Sb_2Se_3 single crystals were grown by a modified Bridgman technique [19]. High purity Sb and Se shots (99.999%) were sealed with correct stoichiometry in a quartz ampoule. The ampoule was heated to 850 °C in a furnace until the selenium vapour disappeared, which lasted around three days. Subsequently, the sample was cooled down slowly to 450 °C and kept at this temperature for three days. Finally, the ampoule was quenched to room temperature in air. The phase purity and the cell parameters were checked by powder x-ray diffraction using a STOE STADIP diffractometer and Cu $K_{\alpha 1}$ radiation ($\lambda = 1.54051$ Å). The obtained crystals were cut in roughly 2×4 mm large pieces for the experiments. In Fig. 1(c), a light microscope image of a crystal is shown and the needle-like, brittle structure can be recognized. According to a combined STM, AFM, and LEED study [19] the ribbon direction was found to be *perpendicular* to the macroscopic needle direction. In reciprocal space, the direction along ribbons corresponds to the ΓY direction while the ΓZ direction is perpendicular to the ribbons. In photoemission, the probing depth is rather short and therefore clean and well-defined surfaces are required. In order to achieve this, the samples were cleaved in ultra-high vacuum (UHV) between (100) planes, which are only bonded by weak van der Waals forces, using a scotch tape [4,20]. The cleavage plane is indicated in the crystal structure in Fig. 1(a). By checking the residues on the tape it can be ensured that a closed layer was removed. All measurements were carried out at room temperature under UHV conditions at a base pressure below 5×10^{-10} mbar.

B. Experimental setup

For the time-resolved photoemission experiments, a commercial mode-locked Ti:sapphire oscillator with a regenerative pulse amplifier (Coherent Mira Seed and RegA9050) was used. This system emits ultrashort laser pulses with a pulse duration of about 50 fs full width at half maximum and a pulse energy of 6 μJ with a tunable wavelength between 780-830 nm. The repetition rate was set to 100 kHz and the wavelength to 830 nm for the measurements. In a nonlinear β-barium borate (BBO) crystal, the fundamental was frequency-doubled to 415 nm or 3.0 eV and split into a pump and probe beam using a beamsplitter. While the pump beam was guided over a computer-controlled delay stage the probe beam was again frequency-doubled in a second BBO crystal to 208 nm or 6.0 eV and the group velocity dispersion was compensated in a CaF_2 prism compressor. Both beams were recombined by a dichroic mirror and focused collinearly onto the sample in the UHV system. The $1/e^2$ waist of the 415 nm pump beam on the surface was determined on a fluorescent yttrium-aluminium-garnet (YAG) sample with a charge-coupled device (CCD) camera as 500 μm. The temporal width of the cross-correlation function was measured on a short-lived intermediate state ($\tau = 30$ fs) on a unreconstructed, clean $Cu_2O(111)$ single crystal as 90 fs full width at half maximum. The polarization of the beams can be adjusted with $\lambda/2$ waveplates. For the measurements the electric field vector of the light was aligned either parallel or perpendicular to the ribbon direction. Incident pump fluences below $\Phi_{max} = 36\ \mu J/cm^2$ were used, which correspond to excitation densities in the order of $2.1 \times 10^{19}\ 1/cm^3$ for an optical absorption length of 16 nm and a reflectivity of 57% [21]. The photoemitted electrons were detected according to their kinetic energy and emission angle in a commercial hemispherical electron energy analyzer (Specs Phoibos 100) with a two-dimensional detector. The acceptance angle of the detector is ±15° [22]. An upper limit for the energy resolution was determined by the full width at half maximum of the surface state in the valence band spectrum of Ag(111) measured with 6 eV light as 65 meV. The sample was oriented in a way that the ribbons are aligned either parallel or perpendicular to the entrance plane of the detector, so that the band structure along ΓY or ΓZ can be mapped, respectively. The Fermi level was measured on a silver crystal. Due to the irregular structure of the cleaved surface the angle of normal emission was determined at the apex of the secondary electron cut-off. For the low pump fluences used, no time-dependent shift of the spectrum due to space charge or surface photovoltage effects was observed.

The valence band spectrum was measured with a monochromatic high harmonics generation (HHG) light source with a photon energy of 15.5 eV. In this source, the fundamental beam with a wavelength of 800 nm at a repetition rate of 100 kHz is frequency doubled in a BBO crystal to 400 nm or 3.1 eV and focused into an argon-gas jet. In the gas jet, the fifth harmonic of the driving laser frequency is produced. The fundamental is blocked by a 200 nm indium filter. The divergent beam is collimated by a spherical mirror and focused onto the sample with a toroidal mirror [23]. Because light in the extreme ultraviolet range below 200 nm is absorbed in air the high harmonics generation and the beam path towards the sample are in UHV at a base pressure below 5×10^{-9} mbar. The $1/e^2$ beam waist of the HHG source was again determined on a fluorescent YAG sample as 220 μm [23], which is smaller than the sizes of the samples and of the pump beam.

C. Computational details

The electronic band structure of Sb_2Se_3 was calculated via the density functional theory, within the generalized gradient approximation (GGA) of the Perdew-Burke-Ernzerhof (PBE) realization [24], as implemented in the Vienna *ab initio* simulation package (VASP) [25,26]. The projector augmented wave (PAW) pseudopotentials were adopted for the calculation [27,28]. Electrons belonging to the outer atomic configuration were treated as valence electrons, here corresponding to five electrons in Sb ($5s^2 5p^3$) and six electrons in Se ($4s^2 4p^4$). The plane-wave cutoff energy was set to 500 eV. The Γ-centered k-point mesh of size $6 \times 20 \times 7$ was used for the Brillouin-zone sampling. Spin-orbit coupling was included in our calculations.

III. RESULTS

A. Electronic valence band structure

Angle-resolved photoelectron spectroscopy (ARPES) measurements were carried out in order to investigate the electronic valence band structure of a cleaved $Sb_2Se_3(100)$ surface using the HHG light source with a photon energy of $h\nu = 15.5$ eV. The dispersion along the crystallographic directions along and across ribbons are compared, corresponding to ΓY and ΓZ in reciprocal space, respectively. The light was p-polarized and the parallel component of the electric field vector was aligned along the ribbons in the first case and perpendicular to the ribbons in the second case. The measured spectra integrated in momentum from 0–0.35 $Å^{-1}$ along the corresponding symmetry directions are shown together with a detailed view on the valence band maximum (VBM) and the calculated band structure in Fig. 2. The VBM was found along ΓZ and the onset was determined as $E_{\mathrm{VBM}} - E_F = (-0.67 \pm 0.10)$ eV with respect to the Fermi level E_F. A shift of the onset for the spectrum along ΓY towards $E_{VB,\Gamma Y} - E_F = (-0.74 \pm 0.10)$ eV was observed. The work function can be extracted from the center position of the rising edge of the low-energy secondary electron cutoff E_{Onset} as $\Phi = h\nu - (E_F - E_{\mathrm{Onset}}) = (4.57 \pm 0.14)$ eV. These values are in good agreement with the calculated band structure, which is shown in Fig. 2(b), and previously published data [6,19]. Additionally, as already reported in the first ARPES study on crystalline Sb_2Se_3 [6], depending on the direction of the electric field vector with respect to the ribbon direction changes in the relative peak intensities in the VB spectra are observed.

B. Tr-2PPE along ΓY and ΓZ

In order to determine the conduction band electronic structure and the relaxation dynamics of photoexcited charge carriers, time-resolved two-photon photoemission (tr-2PPE) experiments were performed. Electrons are excited from the VB to the CB by absorption of 3 eV pump photons from where they can be photoemitted by a 6 eV probe pulse. The two-dimensional electron detector allows the population in the lower conduction bands to be mapped within a momentum window of ± 0.15 $Å^{-1}$ either along ΓY or ΓZ for each time delay. The polarization of the pump light was adjusted in a way that the parallel component of the electric field vector points always along the ribbon direction, more precisely it was p-polarized in case of ΓY and s-polarized in case of ΓZ. For the tr-2PPE data, the equilibrium energy distribution was subtracted, which was obtained from the raw data by averaging the data at negative time delays where the probe pulse precedes the pump pulse. This correction allows to

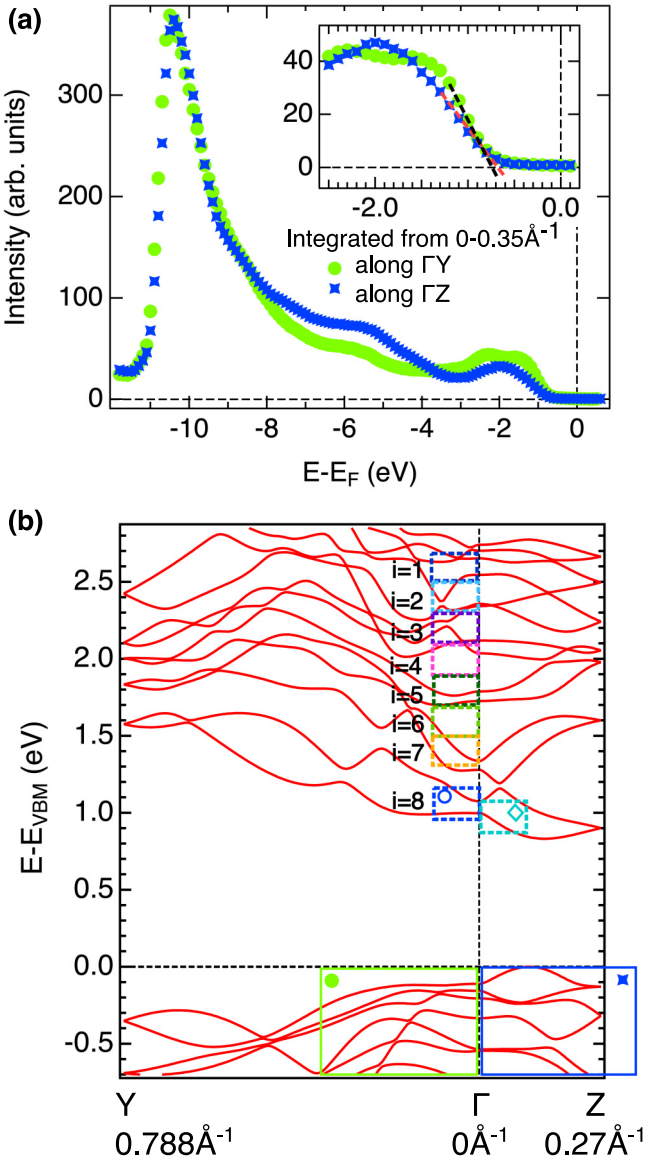

FIG. 2. (a) Valence band spectra along ΓZ (dark-blue crosses) and ΓY (light-green dots) measured with the HHG light source and using a photon energy of 15.5 eV. A bias voltage of −5 V was applied to the sample with respect to the analyzer. The spectra are integrated from 0–0.35 $Å^{-1}$ along the corresponding symmetry directions. The inset shows a detailed view on the valence band onsets. The energy positions of the onsets are indicated by linear fits. The electric field vector of the light was aligned along the ribbons for the ΓY direction and perpendicular to ribbons for the ΓZ direction. (b) First-principles calculations of the band structure of Sb_2Se_3 along ΓY (parallel to the ribbons) and ΓZ (perpendicular to the ribbons). The regions where the valence band spectra in (a) were taken are marked as colored boxes. Besides, the regions where the conduction band dynamics is analyzed are marked as dashed boxes.

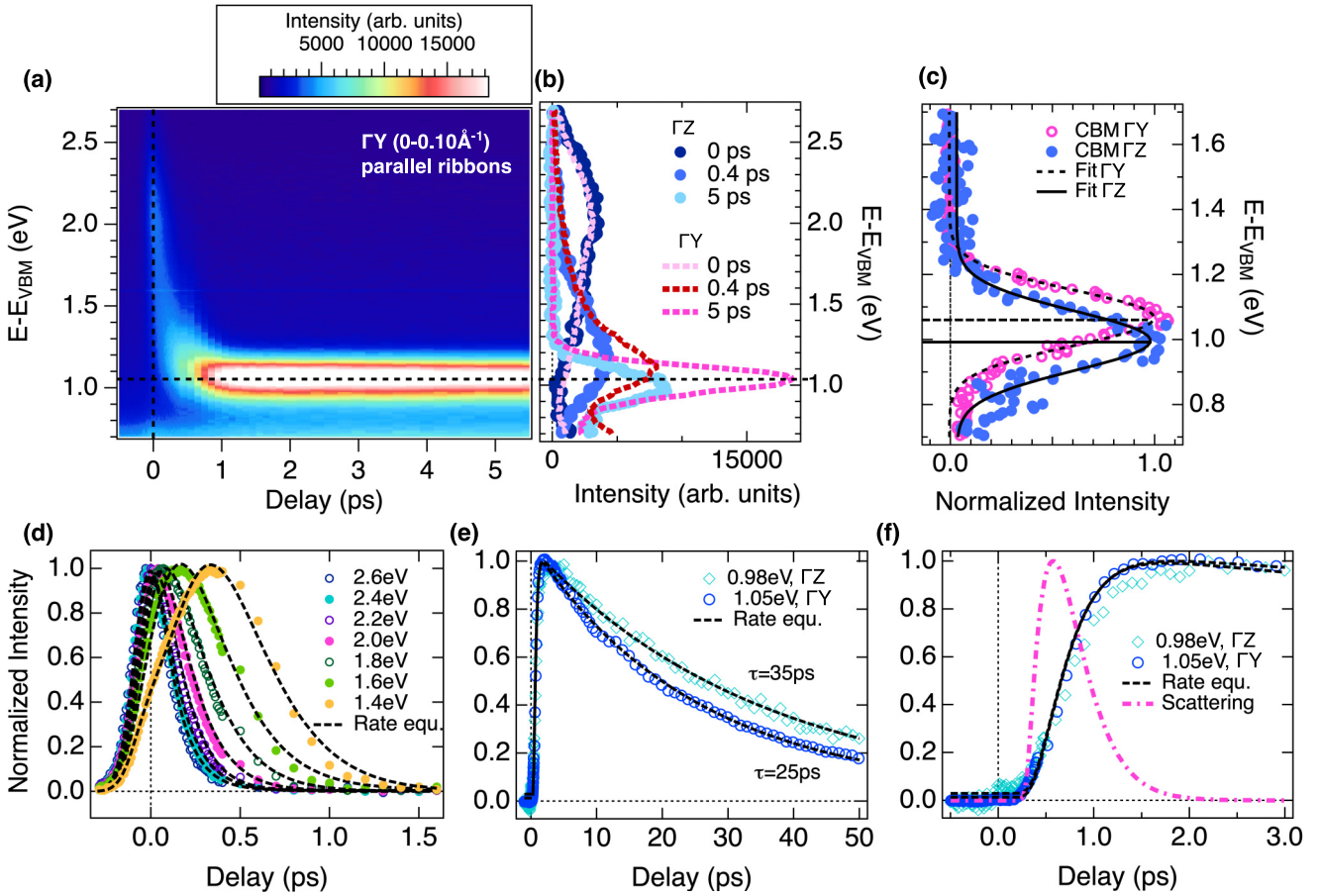

FIG. 3. (a) Energy distribution integrated from 0–0.10 Å^{-1} in ΓY direction. (b) Spectra taken at selected time delays integrated from 0–0.10 Å^{-1} in ΓY direction (red and pink dotted lines) and in ΓZ direction (blue symbols). The spectra along ΓZ were multiplied by a factor of 4.5. (c) Nonintegrated spectra taken after 3 ps at 0.10 Å^{-1} from Γ towards Y at the local CBM (blue dots) and towards Z at the global CBM (pink circles). Gaussian fits are superimposed to the measured data (black lines). [(d)–(f)] Intensities at selected energies E_i integrated in the range of $E_i \pm 0.1$ eV and in momentum from 0–0.10 Å^{-1} as a function of the time delay. Fit results according to rate equations are superimposed (black dashed). The data were normalized to the maximum intensity. The time-dependent population in the local conduction band minimum along ΓY and the global conduction band minimum along ΓZ are compared in (d) on a longer and in (e) on a short timescale. In (e), the trace due to scattering from energetically higher states into the CBM is superimposed.

remove the structureless and delay-independent background signal of thermally excited electrons and makes the measured, pump-induced features better recognizable. The integration time for each data point was 50 s for the data along ΓY and 5 s along ΓZ.

The time-dependent energy distribution of photoexcited electrons in the CB along the ΓY direction is shown in Fig. 3(a), integrated in momentum from $\overline{\Gamma}$ up to 0.10 Å^{-1} towards Y. For short time delays the occupation of several conduction band states is observed. Within less than 1 ps an ultrafast decay into the band minimum occurs, where the lifetime increases to a few tens of picoseconds. Based on the spectra taken along ΓY and ΓZ at selected times after excitation, shown in Fig. 3(b), slightly anisotropic relaxation processes are recognizable. At the moment of excitation no difference between ΓY (dark-blue circles) and ΓZ (light pink dashed line) was found except for a smaller photoemission yield in the latter case. To take this into account, all spectra along ΓZ are multiplied by a factor of 4.5 so that the intensities of spectra at the moment of excitation are normalized. In both cases, conduction bands from about 1.0–2.7 eV above the VBM are populated. Within the first 400 fs the highest conduction bands decay completely into energetically lower lying states where a strong increase in occupation can be observed. There is a difference in the relative peak positions and intensities in the spectra along and perpendicular to the ribbon direction, with a lower total intensity along ΓZ. After several picoseconds all electrons have accumulated in the lowest conduction band and the energy position of the band minima in both directions can be determined. Based on the angle-resolved data shown in Fig. 4 the global conduction band minimum (CBM) was found at about 0.1 Å^{-1} from Γ towards Z and a local CBM at 0.1 Å^{-1} towards Y. The nonintegrated spectra, which were taken at this positions after 3 ps are shown in Fig. 3(c). The indirect band gap at room temperature can be determined by referencing the maximum position of the peak along ΓZ to the VBM as $E_{\text{gap}} = 0.99$ eV. The VBM was found at 0.10 Å^{-1} away from Γ towards Z. This shows that the offset between VBM and CBM is very small. For the local CBM along ΓY, the energy difference in respect

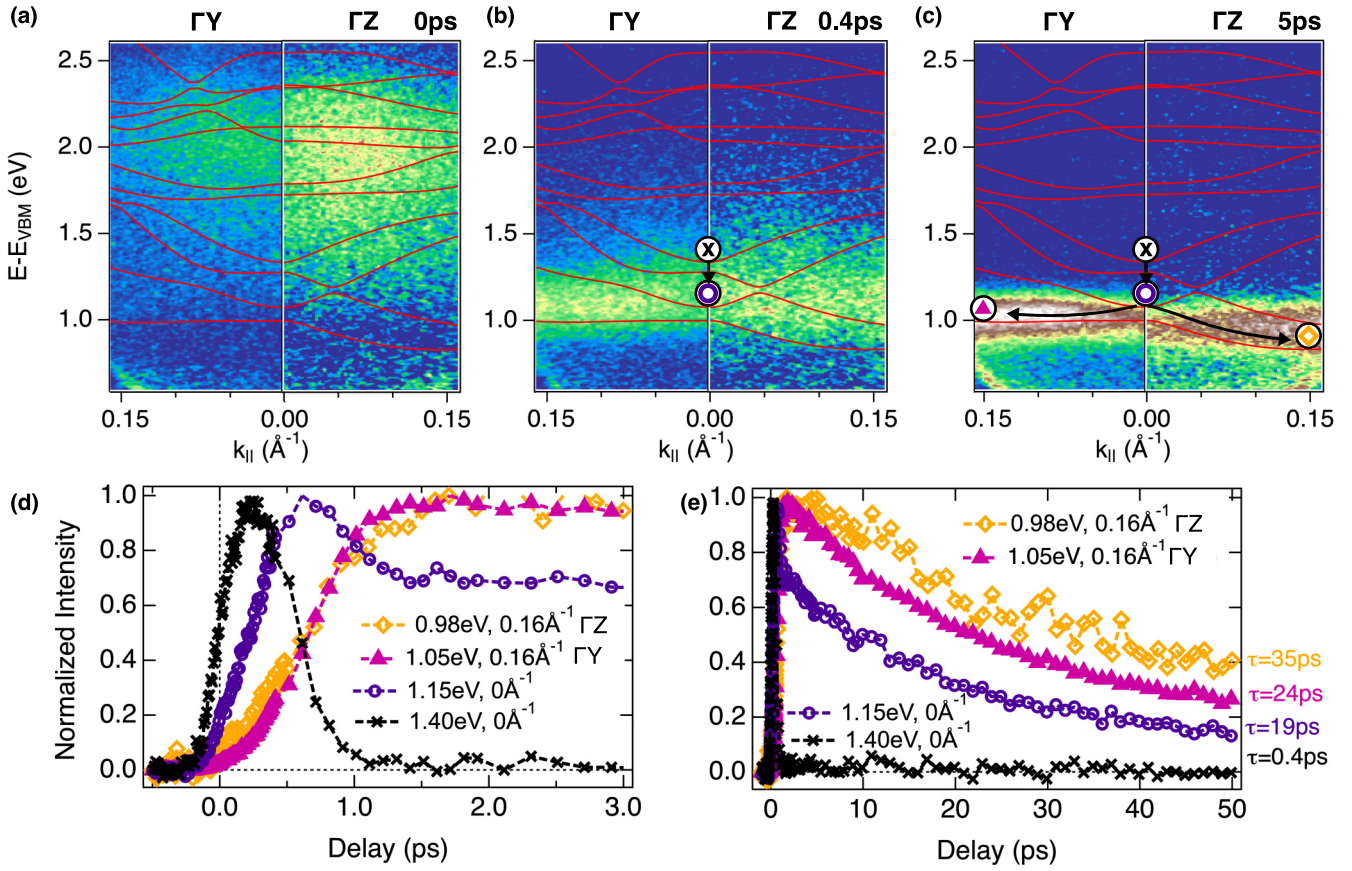

FIG. 4. (a) Energy and momentum distributions of photoexcited electrons in the conduction bands along ΓY and ΓZ at the moment of excitation, after (b) 0.4 and (c) 5 ps. The differences in the relative intensities are due to transition matrix element effects. The calculated band structure is superimposed for each time step. The symbols in (b) and (c) show the pathway of decaying electrons. (d) Normalized transient electron population on a short and (e) on a longer timescale taken at the energy and momentum positions marked in (b) and (c).

to the VBM is slightly larger with $E_{\mathrm{CBM},\Gamma Y} - E_{\mathrm{VBM}} = 1.07$ eV. The obtained band gap coincides well with values reported in literature [1] and the dispersion is in agreement with the calculated band structure, which is shown in Fig. 2(b).

The intensities at arbitrarily chosen energies E_i integrated in the range of $E_i \pm 0.1$ eV and in momentum from 0–0.10 $\mathrm{Å}^{-1}$ along ΓY are plotted as a function of time delay in Figs. 3(d)–3(f). The related integration regions for each E_i are marked in the calculated band structure in Fig. 2(b). With decreasing energy a shift of the maximum position towards longer delays accompanied by an increase in temporal width is observed.

A quantitative description of the time-dependent population can be achieved by applying rate equations to the occupations N_i in the related states at E_i for $i = 1, 2, \ldots, 8$. By assuming that all states can be populated directly by the pump pulse at $\mathrm{t} = t_0$ and all energetically higher lying states E_k can decay into lower lying states at energies E_i for $k < i$ this gives the following equations:

$$\frac{dN_1}{dt} = A_1 \exp\left[-\frac{(t-t_0)^2}{2\sigma_L^2}\right] - \frac{N_1}{\tau_1}, \tag{1}$$

$$\frac{dN_i}{dt} = A_i \exp\left[-\frac{(t-t_0)^2}{2\sigma_L^2}\right] - \frac{N_i}{\tau_i} + \sum_{k=1}^{i-1} B_k \frac{N_k}{\tau_k} \tag{2}$$

for $i = 2, 3, \ldots, 8$. The lifetime of photoexcited electrons in state E_i is denoted as τ_i and A_i means the number of electrons excited by the pump pulse into this state. $B_{k,i}$ describes the fraction of electrons that decays from an energetically higher lying state at E_k with a lifetime τ_k into the state i at E_i. Besides, σ_L is the temporal width of the pump pulse, which was determined from the fit of the energetically highest state at E_1 and the obtained value of 70 fs was kept constant for all other states. Consequently, the fitting parameters in Eq. (2) are A_i, τ_i, and $B_{k,i}$. In order to reduce the number of fitting parameters, just one state k was considered to decay into a state i. The respective state k was chosen according to the best fit result. Only for the state E_7 at 1.4 eV it was necessary to consider two states k in order to obtain a good fit result. Furthermore, the intensity in the energy window E_7 is modulated by the high energy tail of window E_8 comprising the intense CBM. This was taken into account by subtracting the transient at E_8 after proper scaling using a multiplication factor of 0.08. In Figs. 3(d)–3(f), the fit results according to these rate equations are superimposed as black dashed curves. It can be recognized that the measured transients can be described rather well with this model.

The population in the highest conduction bands $E_1 - E_4$ at $E - E_{\mathrm{VBM}} = 2.6$–$2.0$ eV decays fast within 110 fs. For the energies $E_5 - E_7$ ($E - E_{\mathrm{VBM}} = 1.8$–$1.4$ eV), the lifetime is

still rather short and increases with decreasing energy from about 200 to 300 fs. In the lowest CB a long lifetime of 25 ps was obtained. For the lower energies (E_{3-8}), scattering from energetically higher states into these states has to be taken into account, whereas it is neglectable for E_2. This leads to a time delayed rise of the population in the energetically lower states. It was found that for the lowest CB, scattering arises mostly from states around 1.4 eV. The corresponding source term is shown in Fig. 3(f) together with the transient of the lowest CB. The maximum population is reached well after the first picosecond, and only a small fraction of the population can be attributed to a direct excitation by the pump pulse. It can be recognized that all transients can be well described by the model, which just includes scattering events from one energetically higher state. Only for the transient at 1.4 eV scattering from two states had to be considered. No clear contribution of a transport of photoexcited charge carriers from the bulk to the surface due to the electric built-in field was observed in contrast to recent results obtained from Cu_2O [18]. Within the band gap no evidence of surface defect states was found. Except for differences in the photoemission yield, no influence of the light polarization on the charge carrier dynamics was observed (data not shown).

In order to investigate whether the anisotropic character of Sb_2Se_3 is also reflected in the charge carrier relaxation, the same measurement was carried out along ΓZ, corresponding to the direction perpendicular to the ribbons. In this case, the pump light was *s*-polarized, so that the parallel component of the electric field vector points again along the ribbon direction. As a consequence, variations in the relative intensities can occur due to changes of the transition matrix elements, which can be observed in Fig. 3(b). For the relaxation of charge carriers in energetically higher conduction bands, no major differences between both directions were recognized. The lifetime in the highest states is also 110 fs and increases with decreasing energy to about 300 fs. At the global CBM, which was found at about 0.10 $Å^{-1}$ along ΓZ, the longest lifetime of 35 ps was observed. This can be explained by the fact that for those electrons recombination is the only possible relaxation channel. In contrast to that, for electrons in the local and rather shallow minimum along ΓY either recombination or scattering towards the global minimum is still possible and thus, the depopulation is faster. The time-delayed population of energetically lower lying states can again be explained by scattering from higher states into those states. For the CBM, the respective transients for both directions are compared in Figs. 3(e) and 3(f). The fit results based on rate equations are superimposed to the measured transients. It can be seen that the rise of the population in the lowest CB is rather similar for both directions. Finally, the only difference between the ΓY and the ΓZ directions found in our data is the slightly longer lifetime in the global CBM along the ΓZ direction.

In Figs. 4(a)–4(c), the energy and momentum distribution of photoexcited charge carriers along ΓY and ΓZ at the moment of excitation, after 0.4 and 5 ps are shown. The calculated band structure is superimposed to the measured data. The variations in the relative intensities for the two directions are due to different light polarizations. A good agreement between the calculated band structure and the measurements is observable and allows the reconstruction of the relaxation pathways of excited charge carriers. At the moment of excitation mostly energetically higher states around 2.0 eV are occupied. Within the first hundreds of femtoseconds scattering into energetically lower lying states leads to an accumulation of the electrons in the lowest conduction bands. There, scattering from $\overline{\Gamma}$ towards the local and global conduction band minima occurs, which are located about 0.10 $Å^{-1}$ along both, ΓY and ΓZ. The time-dependent normalized populations at four different energy and momentum locations are compared on two different timescales in Figs. 4(d) and 4(e). The corresponding points are marked in Figs. 4(b) and 4(c). At $\overline{\Gamma}$, 1.40 eV above the VBM, the maximum population due to scattering is reached already 300 fs after excitation and a short lifetime of about 300 fs is observed. At the lowest conduction band at $\overline{\Gamma}$ the maximum population appears later, at about 600 fs after excitation, and it takes roughly 1 ps more until the highest population in the local and global CBM is reached. The lifetime of charge carriers in the lowest CB at $\overline{\Gamma}$ is 19 ps, which is slightly shorter than in the band minima along ΓY and ΓZ. Again, the faster depopulation can be explained by additional relaxation channels into the conduction band minima.

IV. DISCUSSION

Time-resolved photoemission experiments were conducted in order to investigate the electronic structure and the relaxation dynamics of photoexcited electrons in Sb_2Se_3(100). The directions along and across ribbons, corresponding to ΓY and ΓZ, respectively, are compared. In both cases, the same conduction bands could be populated. The energetically higher states decay fast in about 100–300 fs due to scattering into energetically lower lying states. Within the first hundreds of femtoseconds scattering towards the lowest conduction band occurs, followed by momentum scattering towards the band minima along ΓY and ΓZ in the subsequent picosecond. There, rather long lifetimes of 25 and 35 ps are observed. In our measurements, no evidence for trapping due to surface defect states within the band gap was found.

The one-dimensional structure of Sb_2Se_3 is reflected in anisotropic physical properties [1]. Therefore it would be conceivable that the charge carrier dynamics show anisotropic features as well. Nevertheless, almost no difference along ΓY and ΓZ within the investigated region was observed. This might be due to the fact that the electronic structure close to the VBM is quite similar in both directions in the vicinity of $\overline{\Gamma}$. The lifetime in the global CBM along ΓZ is longer than in the local and shallow minimum along ΓY. This can be explained by an additional relaxation channel for electrons in the local band minimum, which can either scatter into the global CBM or recombine. However, for electrons in the global minimum recombination is the only relaxation channel possible and thus the lifetime is slightly longer. In comparison to other semiconductors like silicon, where the local conduction band minimum scatters within 180 fs towards the global minimum [29], the intervalley scattering in Sb_2Se_3 seems negligible because the lifetimes in both minima are similar. The deformation potential of polar semiconductors like Sb_2Se_3 is in general larger than for silicon that should

cause a faster intervalley scattering. Nevertheless, based on temperature-dependent terahertz spectroscopy measurements [30], it was observed that phonon-scattering related to a deformation potential is unlikely in Sb_2Se_3. Besides, the energy difference between the two minima is quite small and at some point the scattering processes in both directions become similarly probable.

For the use of Sb_2Se_3 in solar devices like in thin-film solar cells or photoelectrochemical cells, efficient charge carrier transport towards the surface or interface is mandatory. Moreover, long lifetimes at sufficiently high energies are required in order to obtain high charge injection rates into adjacent media. In the presented tr-2PPE study, a long-living population in the CBM at the surface was observed. The measured decay constant of 35 ps is in agreement with the values obtained in time-resolved terahertz spectroscopy measurements on nanostructured $Sb_2Se_3/TiO_2/RuO_x$ photocathodes in Ref. [16] or polycrystalline thin film samples in Ref. [17] at similar pump fluences. Furthermore, the decay constants of 100–300 fs for the energetically higher conduction bands are in agreement with the values reported in Ref. [17]. This suggests that neither the nanostructured morphology of the electrodes nor grain boundaries have a major influence on the lifetime of charge carriers in the CB. Owing to the high surface sensitivity, tr-2PPE probes the lifetime of photoexcited charge carriers near the surface, whereas in time-resolved terahertz spectroscopy a deep layer of the bulk sample is probed. The similarity of the results shows that the relaxation is nearly unaffected by surface defects and is determined by charge carrier interaction. This was already proposed in Ref. [17] where no dependence of the lifetime in the CB on the thickness of thin-film samples could be observed. Due to the higher time-resolution combined with the additional energy and momentum resolution in tr-2PPE, those decay constants can now be attributed to distinct electronic states and underlying relaxation processes can be fully characterized. Based on our analysis, no clear evidence for transport of excited charge carriers from the bulk towards the surface was found.

In comparison to Cu_2O, another promising material for solar energy conversion, these results show different bahavior. In Ref. [18], tr-2PPE measurements on $Cu_2O(111)$ single crystals are presented for different surface defect densities. In the case of a low defect density, the authors observed an efficient transport of photoexcited charge carriers in the CB from the bulk towards the surface, where relaxation with a decay constant of 20 ps takes place. By increasing the surface defect density, an efficient trapping in defect states is reported so that no population of the CB close to the surface could be observed and the spectra were dominated by long-lived defect states within the band gap. In contrast, in Sb_2Se_3 no clear contribution of charge carrier transport from the bulk towards the surface was found. This would cause a time-delayed population of the investigated states close to the surface. Based on our analysis, the time-delayed population of energetically lower lying states could be well explained by scattering from higher states without the need to include an additional population due to transport. Furthermore, the decay of the conduction band population is exponential and considerably slower with a lifetime of 35 ps and no major influence of surface defects was found.

Bulk and surface defects form states within the band gap of a semiconductor and trapping in defect states reduces the mobility of charge carriers because thermally activated hopping between equivalent sites is the only transport mechanism possible. The defect states in Sb_2Se_3 were investigated by means of deep-level transient spectroscopy (DLTS) measurements in Ref. [31]. The authors observed mid-gap states and attributed the low photovoltages to trapping of charge carriers in the related defects. In addition, in Ref. [17], the diffusion length of trapped charge carriers was determined and it was found that these are also transported to the surface and contribute to the photocurrent of the cell. According to first-principles calculations the most likely defects are cation-anion and anion-cation antisites which form states at about 0.5 and 0.7 eV above the VBM [32], in agreement with the energy positions found in DLTS. Moreover, in one-dimensional systems and in materials with a small elastic constant but strong electron-phonon coupling a self-trapping mechanism is predicted [33]. Small deformations of the lattice induced by the carriers themselves may lead to local potential barriers, which can trap charge carriers. Such a polaronic self-trapping mechanism was already considered in amorphous and crystalline Sb_2S_3 samples in Ref. [34]. There, the authors observed such high densities of defect states in their measurements, which exceeded the intrinsic defect concentration by far, and they ascribed this to the formation of additional defects by the self-trapping mechanism. In Sb_2Se_3, also large defect concentrations were found in Refs. [16,17] in fluence- and temperature-dependent terahertz spectroscopy measurements, which clearly exceed the intrinsic defect concentrations. Thus, also in Sb_2Se_3, self-trapping might occur. Interestingly, no defect states were observed in our tr-2PPE measurements. This might be due to the low concentration of intrinsic defects combined with the high surface sensitivity of this method since self-trapping is only possible in the bulk and recombination occurs once the self-trapped charge carriers reach the surface.

Summarizing, tr-2PPE measurements on the (100) surface of cleaved Sb_2Se_3 crystals are presented. Due to photoexcitation conduction bands up to 2.7 eV above the VBM can be populated. Ultrafast decay into the lowest conduction band occurs and the charge carriers accumulate in the band minima, where they have long lifetimes of up to 35 ps, which is almost twice as long as in Cu_2O. On our high-quality single crystalline samples defect scattering seems to be negligible. Surprisingly, the anisotropic nature of Sb_2Se_3 has no strong effects on the charge carrier dynamics. These findings should contribute to a better understanding of this promising material for solar energy applications and its behavior under illumination.

ACKNOWLEDGMENTS

The research was funded by the Swiss National Science Foundation under Grant No. 200020_172641 and by the University of Zurich through the Research Priority Project LightChEC.

[1] K. Zeng, D.-J. Xue, and J. Tang, Semicond. Sci. Technol. **31**, 063001 (2016).

[2] E. Dönges, Z. Anorg. Allg. Chem. **263**, 280 (1950).

[3] N. W. Tideswell, F. H. Kruse, and J. D. McCullough, Acta Crystallogr. **10**, 99 (1957).

[4] H. Song, T. Li, J. Zhang, Y. Zhou, J. Luo, C. Chen, B. Yang, C. Ge, Y. Wu, and J. Tang, Adv. Mater. **29**, 1700441 (2017).

[5] S. D. Shutov, V. V. Sobolev, Y. V. Popov, and S. N. Shestatskii, Phys. Status Solidi (b) **31**, K23 (1969).

[6] Z. Hurych, D. Buczek, C. Wood, G. Lapeyre, and A. Baer, Solid State Commun. **13**, 823 (1973).

[7] C. Chen, D. Bobela, Y. Yang, S. Lu, K. Zeng, C. Ge, B. Yang, L. Gao, Y. Zhao, M. Beard, and J. Tang, Front. Optoelectron. **10**, 18 (2017).

[8] Y. Zhou, L. Wang, S. Chen, S. Qin, X. Liu, J. Chen, D.-J. Xue, M. Luo, Y. Cao, Y. Cheng, E. H. Sargent, and J. Tang, Nat. Photonics **9**, 409 (2015).

[9] Y. Rodríguez Lazcano, L. Guerrero, O. Gomez Daza, M. T. S. Nair, and P. K. Nair, Superficies y Vacío **9**, 100 (1999).

[10] Z. Li, X. Liang, G. Li, H. Liu, H. Zhang, J. Guo, J. Chen, K. Shen, X. San, W. Yu, R. E. I. Schropp, and Y. Mai, Nat. Commun. **10**, 125 (2019).

[11] C. Chen, Y. Zhao, S. Lu, K. Li, Y. Li, B. Yang, W. Chen, L. Wang, D. Li, H. Deng, F. Yi, and J. Tang, Adv. Energy Mater. **7**, 1700866 (2017).

[12] N. J. Jeon, J. H. Noh, W. S. Yang, Y. C. Kim, S. Ryu, J. Seo, and S. I. Seok, Nature (London) **517**, 476 (2015).

[13] P. Gao, M. Grätzel, and M. K. Nazeeruddin, Energy Environ. Sci. **7**, 2448 (2014).

[14] L. Pan, J. H. Kim, M. T. Mayer, M.-K. Son, A. Ummadisingu, J. S. Lee, A. Hagfeldt, J. Luo, and M. Grätzel, Nat. Catal. **1**, 412 (2018).

[15] A. Paracchino, V. Laporte, K. Sivula, M. Grätzel, and E. Thimsen, Nat. Mater. **10**, 456 (2011).

[16] W. Yang, S. Lee, H.-C. Kwon, J. Tan, H. Lee, J. Park, Y. Oh, H. Choi, and J. Moon, ACS Nano **12**, 11088 (2018).

[17] K. Wang, C. Chen, H. Liao, S. Wang, J. Tang, M. C. Beard, and Y. Yang, J. Phys. Chem. Lett. **10**, 4881 (2019).

[18] L. Grad, Z. Novotny, M. Hengsberger, and J. Osterwalder, Sci. Rep. **10**, 10686 (2020).

[19] R. Totani, F. O. von Rohr, J. Zhao, Z. Novotny, W.-D. Zabka, A. Soluyanov, and J. Osterwalder, Phys. Rev. Mater. **3**, 125404 (2019).

[20] T. D. C. Hobson, O. S. Hutter, M. Birkett, T. D. Veal, and K. Durose, in *Proceedings of the IEEE 7th World Conference on Photovoltaic Energy Conversion (WCPEC) (A Joint Conference of 45th IEEE PVSC, 28th PVSEC & 34th EU PVSEC), Waikoloa Village, HI* (IEEE, 2018), pp. 0818–0822.

[21] C. Chen, W. Li, Y. Zhou, C. Chen, M. Luo, X. Liu, K. Zeng, B. Yang, C. Zhang, J. Han, and J. Tang, Appl. Phys. Lett. **107**, 043905 (2015).

[22] C. Monney, A. Schuler, T. Jaouen, M.-L. Mottas, T. Wolf, M. Merz, M. Muntwiler, L. Castiglioni, P. Aebi, F. Weber, and M. Hengsberger, Phys. Rev. B **97**, 075110 (2018).

[23] A. C. Schuler, Ph.D. thesis, University of Zurich, Zürich, 2018.

[24] J. P. Perdew, K. Burke, and M. Ernzerhof, Phys. Rev. Lett. **77**, 3865 (1996).

[25] G. Kresse and J. Furthmüller, Phys. Rev. B **54**, 11169 (1996).

[26] G. Kresse and J. Furthmüller, Comput. Mater. Sci. **6**, 15 (1996).

[27] G. Kresse and D. Joubert, Phys. Rev. B **59**, 1758 (1999).

[28] P. E. Blöchl, Phys. Rev. B **50**, 17953 (1994).

[29] T. Ichibayashi, S. Tanaka, J. Kanasaki, K. Tanimura, and T. Fauster, Phys. Rev. B **84**, 235210 (2011).

[30] M. Wang, W. Wu, X. Zheng, X. Hou, C. Liu, Q. Hao, and H. Liu, Mater. Lett. **193**, 191 (2017).

[31] X. Wen, C. Chen, S. Lu, K. Li, R. Kondrotas, Y. Zhao, W. Chen, L. Gao, C. Wang, J. Zhang, G. Niu, and J. Tang, Nat. Commun. **9**, 2179 (2018).

[32] C. Savory and D. O. Scanlon, J. Mater. Chem. A **7**, 10739 (2019).

[33] L. D. Landau, Phys. Z. Sowjetunion **3**, 644 (1933).

[34] Z. Yang, X. Wang, Y. Chen, Z. Zheng, Z. Chen, W. Xu, W. Liu, Y. M. Yang, J. Zhao, T. Chen, and H. Zhu, Nat. Commun. **10**, 4540 (2019).